University of Baghdad
College of Engineering
JE
JOURNAL OF ENGINEERING

Journal of Engineering

journal homepage: www.jcoeng.edu.iq

Volume 32 Number 11 November 2026



Plasmon-like Optical–Thermal Coupling in Nano-Engineered Solar Absorber Coatings Integrated Structural, Spectral, and Photothermal Analysis

Saleh K. Jabur [1,*], **Ahmed A. Al-Tabbakh** [2], **Layth AL-Gebory** [3]

[1]Department of Mechanical Techniques, Technical Institute of Basrah, Southern Technical University, Basrah, Iraq
[2]Department of Physics, College of Science, Al-Nahrain University, Baghdad, Iraq
[3]College of Materials Engineering, University of Technology, Baghdad, Iraq

ABSTRACT

This work involves preparing photothermal absorber coatings with nanoparticle additives and their characterization for photo-thermal conversion applications. It includes the correlation between additions of metallic and metal oxide particles, the optical properties of the composite coatings and their photo-thermal conversion characteristics. Coatings incorporating Ni, Fe_3O_4, CuO, NiO, and MnO_2 are characterized using SEM–EDS, UV–Vis spectroscopy (200–1000 nm), specular reflection measurements. The coatings are also subjected to time-resolved photothermal analysis. Ni-incorporated coatings exhibited the highest measured thermal performance among the investigated coatings. A maximum surface temperature of 93.93 °C and stored thermal energy of 213.10 J with a peak heating rate indicator of 0.360 are obtained corresponding to a visible absorption peak at approximately 540 nm. A high spectral absorptance (AUC_α) of about 1.717 and a low reflectivity of 4.6% are also obtained. The results are in agreement with the proposed plasmon-like absorption behavior in metallic Ni nanoparticles that can lead to the transformation of photons into heat. The Fe_3O_4- and CuO-incorporated coatings show competitive performance due to broadband absorption mechanisms. The NiO- and MnO_2-incorporated coatings are found to exhibit lower efficiency due to UV-dominated absorption. Despite its high absorptance, the primary coating thermal response remains limited due to the absence of conductive pathways. Correlation analysis indicates that no individual spectral parameter alone governs photothermal performance. The results demonstrate that effective photo–thermal conversion requires the combined effect of broadband absorption, plasmon-assisted or defect-mediated mechanisms in addition to suitable microstructural characteristics.

Keywords: Composite coatings, Nanostructures, Optical properties, Photo-thermal conversion, Photothermal absorber coatings, Thermal performance.

*Corresponding author
Peer review under the responsibility of University of Baghdad.
https://doi.org/10.31026/j.eng.2026.11.09
This is an open access article under the CC BY 4 license (http://creativecommons.org/licenses/by/4.0/).
Article received: 06/08/2026
Article revised: 05/10/2026
Article accepted: 11/10/2026
Article published: 01/11/2026

1. INTRODUCTION

Direct conversion of solar radiation into heat and electricity with relatively high efficiency and practical scalability has become an increasing requirement for sustainable and high-efficiency energy systems. In photo-thermal conversion systems absorbers play the decisive role in the overall performance of the solar collector. The coatings of these absorbers are designed to have favorable optical and thermal characteristics to maintain high conversion efficiency and low thermal losses. Thus, the goal is to maximize absorptance of the selective coatings. In order to reduce radiative heat losses, solar selective coatings are essentially made to have low thermal emittance in the infrared region and strong absorptance throughout sunlight spectrum, usually in the 0.25–2.5 μm wavelength range **(Kennedy, 2002; Selvakumar and Barshilia, 2012; Duffie and Beckman, 2013; Kalogirou, 2014)**. Because the effectiveness of solar thermal conversion depends on both the absorption of incident radiation and the surface's capacity to hold the absorbed energy, this spectrum selectivity is crucial. As a result, a combined examination of optical absorption and thermal emission behavior is required to assess the photothermal performance of absorber coatings. By adding nanoscale components like metallic nanoparticles and transition metal oxides, recent developments in nanostructured materials have made it possible to significantly improve absorber coatings. Nanostructured systems have enhanced light–matter interaction because of the increase in surface area and the modified optical properties of the nanostructured materials compared to the bulk materials. This can affect significantly the mechanisms of solar absorption and heat transfer **(Cao, 2004; Granqvist, 2007)**. Particularly, the CuO, Fe_3O_4, MnO_2 and NiO have been studied because of their high absorption in the solar spectrum, chemical stability and thermal energy applications **(Kennedy, 2002; Selvakumar and Barshilia, 2012)**. The interaction of the radiation with the coating surface and the heat transfer inside the material are affected by features like particle size, agglomeration state, surface roughness and compositional distribution. The nano-engineered coatings exhibit greater effects, and very slight changes in morphology can result in significant changes in performance **(Goldstein et al., 2018; Farooq et al., 2022)**. Despite the advances in solar absorber materials and the maturity of the solar absorber industry, there remains a great need to gain insight into how structure relates to the photothermal performance of solar absorbers. Numerous studies have tried to correlate the optical properties and the thermal performance. However, a more significant correlation can still be achieved between morphology, composition and energy conversion efficiency. This correlation is crucial to the optimum design of coatings and to performance reliability in actual operating conditions. Modern solar thermal selective coatings have developed to obtain nanostructured and multilayer coatings with enhanced spectrum selectivity obtained by controlling the microstructure and by optimizing material systems to enhance the solar absorption and reduce radiative losses **(Xu et al., 2020; Liu et al., 2021; Al-Obaidy et al., 2024)**. Moreover, for enhanced photothermal conversion efficiency and durability, increasingly complex nanostructuring and material engineering are required to produce solar absorber coatings, as has been recently reported **(Zayed, 2024)**. The investigations have shown that the coating performance is affected not only by the selection of the coating material but also by the fabrication procedure, the design of the structure and the resistance of the coating to degradation under operating conditions. Experimental studies further confirm the importance of nanoscale design to improve the performance of the absorber. In combination with this, nanostructured coatings have been shown to enhance the general energy conversion characteristics, to reduce reflectance, and to increase light–matter

interaction, especially in oxide-based and composite materials **(Wang, 2021; Dawood et al., 2025)**. Likewise, the multilayer and nano-architecture coatings have demonstrated better optical–thermal responsiveness, due to their better control of absorption mechanisms and thermal emission properties **(Rashid et al., 2022)**. Additionally, it has been determined that absorber coating thermal resilience is essential for real-world applications, especially in high-temperature solar systems. Recent studies have shown that it is possible to maintain stable optical properties during long-term exposure to temperature by applying a sophisticated coating technique **(Kumar et al., 2024; Farchado et al., 2024)** thus highlighting the importance of both the choice of materials and the integrity of the structure. The photothermal response has been shown to be affected by the thermal transport within the coating, as well as the optical properties. Coating performance description is not complete using only optical absorption: Research using the photothermal characterization methods has revealed the influence of coating structure and material parameters on heat transfer behavior within the coating absorber layer **(Xu et al., 2020)**. This work utilized several nanopowder technologies for the development of nano-engineered solar absorber coatings such as CuO, Fe_3O_4, MnO_2, Ni and NiO. The systematic evaluation of morphology and elemental content of nanopowders and coatings is carried out using the methods of energy-dispersive X-ray spectroscopy (EDS) and scanning electron microscopy (SEM). The optical behavior is analyzed on the basis of spectral measurements, and experimental tests are performed under controlled irradiation under the photothermal response. In addition, the correlation between the structural characteristics and the KPIs was measured statistically, providing a comprehensive framework for analyzing optical–thermal correlation in nano-engineered coatings. This integrated approach enables the more precise understanding of the mechanisms of photothermal conversion and paves the way to develop high-efficiency solar absorber coatings with improved optical selectivity, thermal stability and performance in solar thermal applications. These are key to creating a greater understanding of nano-engineered solar absorber coatings.

2. MATERIALS AND METHODS

2.1 Primary Coating Layer

The base matrix for preparation of the primary coating layer was obtained from a commercially available HRP (heat resistant paint) based on acrylic materials, which is black painted with carbon black (PBK7). **Table 1** lists some of the paint specifications.

Table 1. Specifications for the heat-resistant paints used

Property	**Paint (Acrylic Spray)**
Resin Type	Fast-drying acrylic resin
Pigment Type	carbon black (PBK7)
Solvent	Water and other voltile organic compounds to accelerate dying
Surface Dry Time	6–8 min
Full Dry Time	≈ 1 hr
Final Finish	Smooth, matte, corrosion resistant
Heat Resistance (°C)	-40 to +170
Application Temp (°C)	+10 to +25
Shelf Life	3 years
Relative Density	0.945±0.08

The coating was chosen because of its thermal stability and as a reference matrix for assessing the effect of the nanostructured additives on the solar absorption and heat accumulation behavior under solar irradiation conditions. Coatings were applied with CuO, Fe_3O_4, MnO_2 and Ni fine powders, in nanometer size, in the coatings. The nanopowders used were all purchased from Sigma-Aldrich (Shanghai), China, and indicated as ≥99% pure.
The nominal primary particle sizes specified by the supplier were ~50 nm for CuO, 30–50 nm for Fe_3O_4, ~50 nm for MnO_2, 50–70 nm for Ni, and 30–50 nm for NiO. These particle sizes were based on the supplier specifications and were not quantitatively determined from the SEM images. The amount of each nanopowder was added to paint at 5 wt.% (nanoparticle-to-paint mass ratio = 5:100) for all the nanocomposite coatings.

2.2 Preparation of Substrates

The substrates used were 1 mm thick aluminum sheets of purity of approximately 95% and size of 5 cm × 5 cm. The substrates were mechanically abraded, cleaned with detergent, rinsed with deionized water and placed in acetone to clean remaining contaminants before coating. The samples were then dried in an oven prior to coating. This cleaning technique provides uniformity of surface conditions and is considered suitable for the work of this study.

2.3 Coating Preparation and Application

A summary of the entire coating procedure is shown in **Fig. 1**. The nanoparticle loading (5 wt.%) in all the nanoparticle modified coatings was fixed based on preliminary trials considering optical absorption and dispersion stability. The mixture was then sonicated for 30 min in an ultrasonic unit operating at power of 120 W ultrasonic power and 100 W heating power (50 Hz) to disperse the particles **(Paredes and Burghard, 2004)**. The resulting suspension was then applied to the prepared aluminum substrates using a pressured air spray machine at an angle of approximately 90° and a distance of 20-25 cm from the surface of the substrate.
The coated samples were left to cure for 12 hours at room temperature and then subjected to thermal treatment for 1 hour at 120°C to ensure the stability of the coating and its proper adherence. This preparation technique provides for a more consistent coating by promoting uniform dispersion of the particles in the coating matrix.

2.4 Characterization and Performance of Coatings

Preliminary inspection and investigation of coating uniformity and particle distribution was performed using a digital optical microscope (CoolingTech) with LED illumination and up to 1600x magnification. Coating thickness was measured with an LS220 thickness gauge (manufactured by Shenzhen Linshang Technology, China) and the results given are an average of five measurements taken at different locations on the coated surface. The average coating thicknesses were approximately 89, 97, 102, 94, 90, and 92 μm for HRP, Ni/HRP, NiO/HRP, Fe_3O_4/HRP, CuO/HRP, and MnO_2/HRP, respectively. The LS220 has a specified accuracy of ≤ ± (3%H + 2 μm), where H is the measured thickness. The scanning electron microscope (SEM) (Inspect S50, FEI, Netherlands) was used to study the as-prepared composite coatings. The elemental composition and spatial distribution were analyzed using energy-dispersive X-ray spectroscopy (EDS) with a Bruker XFlash-6l10 detector mounted on the SEM system. UV–Vis spectroscopy was used in order to study interaction of coatings with the solar radiation and its spectral response. Filmetrics (USA) F20 thin-film measurement

system was used to quantify the reflectance, which allowed investigation of the wavelength-dependent behavior. The coatings were investigated for their photothermal behavior by monitoring the temperature change under solar radiation. To allow the incident radiation to enter each sample, it was placed within glass-covered insulated solar test chamber as shown in **Fig. 2**.

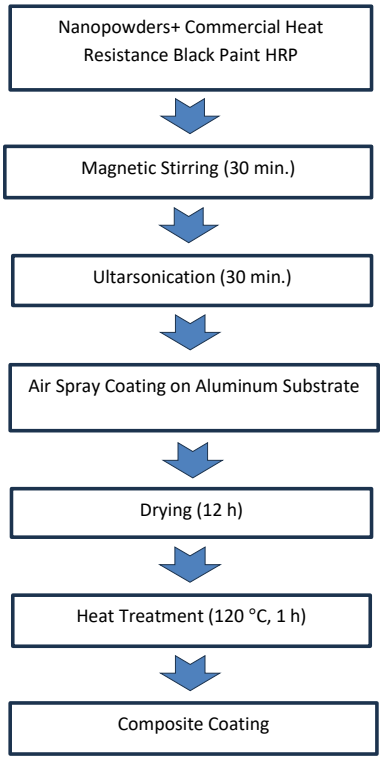


Figure 1. Diagram of the Nanopowder-reinforced composite coating preparation procedure.

A thermocouple attached to a GM1312 digital thermometer (Benetech, China) was used to record surface temperature. The thermometer has a specified accuracy of ± (0.1% of reading + 0.6°C) and a resolution of 0.1°C, while the K-type thermocouple has a Class II tolerance of 2.5°C or 0.75%. The measurements were taken at regular intervals until steady state conditions were achieved. Specular reflectance was measured using a specially designed device that detects the directly reflected solar radiation. The device was configured to detect the directly reflected solar irradiance from the sample along the specular reflection path, while excluding the diffuse component. An SM206-SOLAR power meter (Hangzhou Yucheng Industrial Co., Ltd., China) was used to measure the irradiance. The instrument has a resolution of 0.1 W/m^2 and a specified measurement error of ± (10% of the reading + 2 digits). The angle of incidence was maintained at 45° so that the measurements will be uniform. Three independently prepared specimens were tested for each coating composition. To evaluate measurement reproducibility, each specimen was measured three times, thus giving three independent specimens and three repeated readings per specimen. Reflectance data obtained were then correlated with the UV-Vis data, so as to obtain a comprehensive optical-thermodynamic study.

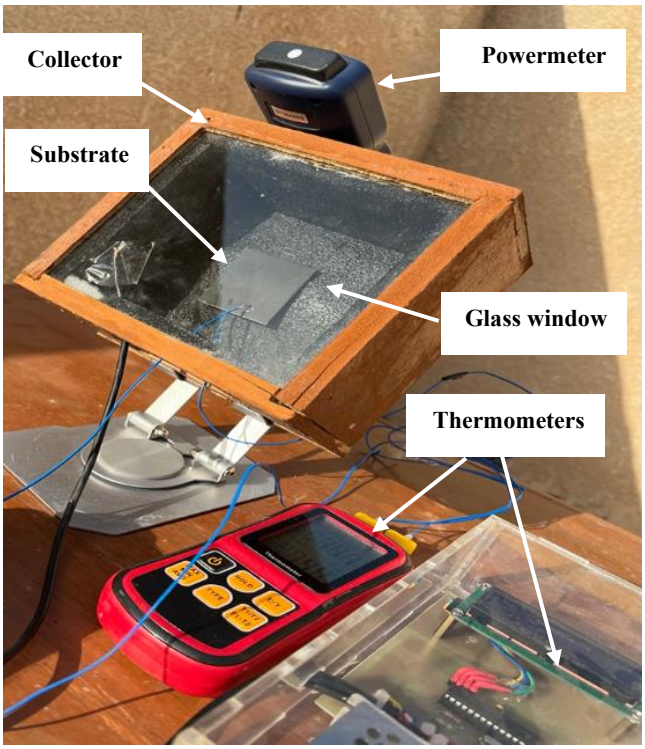


Figure 2. glass-covered insulated solar test chamber

The thermal parameters were calculated as follows:

$$Q_t = mc_p(T_s - T_0) \tag{1}$$

$$\eta_h = \frac{mc_p(dT_s/dt)}{GA} \tag{2}$$

$$\varepsilon_Q = \frac{Q_{t,\text{coating}}}{Q_{t,\text{Al}}} \tag{3}$$

$$\Delta Q_t = Q_{t,\text{coating}} - Q_{t,\text{Al}} \tag{4}$$

$$Q_t^* = \frac{Q_t - Q_{\min}}{Q_{\max} - Q_{\min}} \tag{5}$$

For the reduced-temperature analysis,

$$\eta_h = \eta_0 - F_R U_L \left(\frac{T_s - T_a}{G}\right) \tag{6}$$

where $\eta_0$is the intercept and $F_R U_L$is obtained from the absolute slope (Wm^{-2} K^{-1}). Here, m, c_p, T_s, T_0, T_a, G, and Adenote substrate mass, specific heat capacity, surface, initial and ambient temperatures, solar irradiance, and exposed area, respectively. $Q_t$and ΔQ_t are expressed in J, while η_h, ε_Q, Q_t^*, and $\eta_0$are dimensionless.

3. RESULTS AND DISCUSSION

The SEM images of the nanopowders (CuO, Fe_3O_4, MnO_2, Ni and NiO) are shown in **Fig. 3(a-e)**. The EDS results demonstrate that the dominant elements match the intended compositions, with Cu and O for CuO (80.69 wt.% Cu, 10.62 w.t% O), Fe and O for iron oxide (57.12 wt.% Fe, 26.97 wt.% O), and Mn and O for MnO2 (61.29 wt.% Mn, 24.95 wt.% O). Likewise, NiO nanopowder also exhibits the dominant Ni and O contents (67.63 wt% Ni and 21.40 wt.% O) which confirms that nickel oxide is the predominant compositional phase.

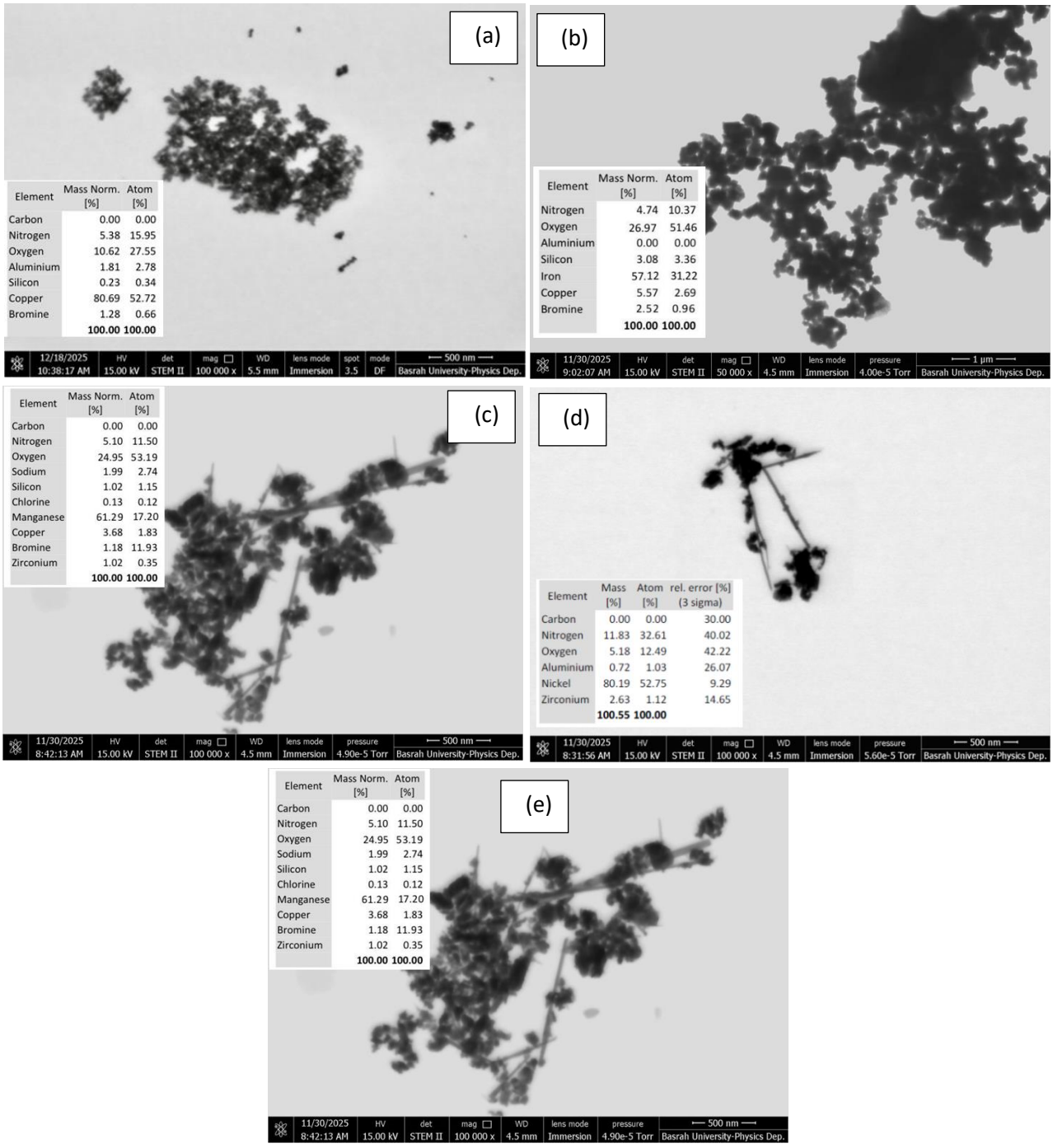


Figure 3. SEM and EDS of Nanopowders. (a) CuO Nanopowder, (b) Fe_3O_4 Nanopowder, (c) MnO_2 Nanopowder and (d) Ni Nanopowder (e) NiO Nanopowder.

The EDS of the Ni Nanopowder exhibited a prominent characteristic Ni, around 7.5-8 keV, indicating nickel is the major constituent of the nanopowder with about (80.19 wt.%) **(Goldstein et al., 2018)**. In addition, small amounts of other elements such as N, Si, Br, Cu, Na and Zr are present in all the samples; these are believed to be trace contamination or residues from handling and sample preparation, and not to be intrinsic to the nanopowders **(Reimer and Kohl, 2008)**.

The structural analysis shows that the nanopowders are mainly present as clustered assemblies. They are made of primary nanounits that are assembled into larger agglomerates with high spatial heterogeneities. Although the particle sizes and extent of aggregation vary between materials, the SEM images show that the dispersion is incomplete in all materials, with irregular and interconnected clusters seen in each image. In particular, Nanopowder Ni exhibits comparatively dense clusters with low degree of separation between the particles of the primary, while in nanopowders based on oxides, there are chain-like clusters and loosely connected agglomerates of fine primary particles. In addition, the NiO nanopowder exhibits irregular and agglomerated cluster-like shapes with connecting nanoscale features that are unevenly distributed across the surface. This difference, however, does not prevent the production of multi-scale agglomerates from the nanoscale units from being the most common structural feature in all the samples **(Williams and Carter, 2009; Cullity and Stock, 2001)**. The combined results of morphology and composition, considered as a whole, provide an appropriate structural framework for further examination. The identification of nanoscale particles that are organized into clustered patterns is indicative of increased effective surface interaction and is significant for understanding the optical absorption/photothermal conversion behavior. This interpretation will be statistically associated with optical and thermal measurements in the following sections, but it is provided solely as a structural observation without suggesting immediate performance enhancement.

The HRP coating's SEM image **(Fig. 4)** shows a rough, uneven surface with dispersed micro-voids and irregular granular characteristics. In polymer-based coatings with dispersed pigments and fillers, where a continuous matrix with non-uniform domains forms, this kind of surface morphology is frequently seen **(Goldstein et al., 2018)**. The existence of an organic polymer matrix and carbon-based colors is compatible with the EDS analysis, showing carbon and oxygen as the dominating elements. The inclusion of inorganic fillers or additives in the coating system is further suggested by the detection of silicon **(Reimer and Kohl, 2008)**. The coating's overall heterogeneous organic–inorganic structure serves as a baseline against which coatings changed with nanoparticles can be compared. In the sections that follow, this structural condition will be linked to optical and photothermal performance. Due to interparticle interactions and high surface energy, the SEM image **(Fig. 5)** displays a heterogeneous surface with agglomerated CuO particle clusters embedded inside the polymer matrix, indicating partial dispersion **(Goldstein et al., 2018)**. CuO incorporation is confirmed by EDS analysis, with Cu (26.40 wt%) and O (23.66 wt%) as significant components, along with carbon (32.85 wt%) representing the polymer matrix and the presence of Si indicating inorganic additions **(Reimer and Kohl, 2008)**. A hybrid organic–inorganic system with localized structural differences is reflected in this agglomerated and heterogeneous structure, which will be correlated with optical and thermal results and may affect light interaction and subsequent photothermal behavior.

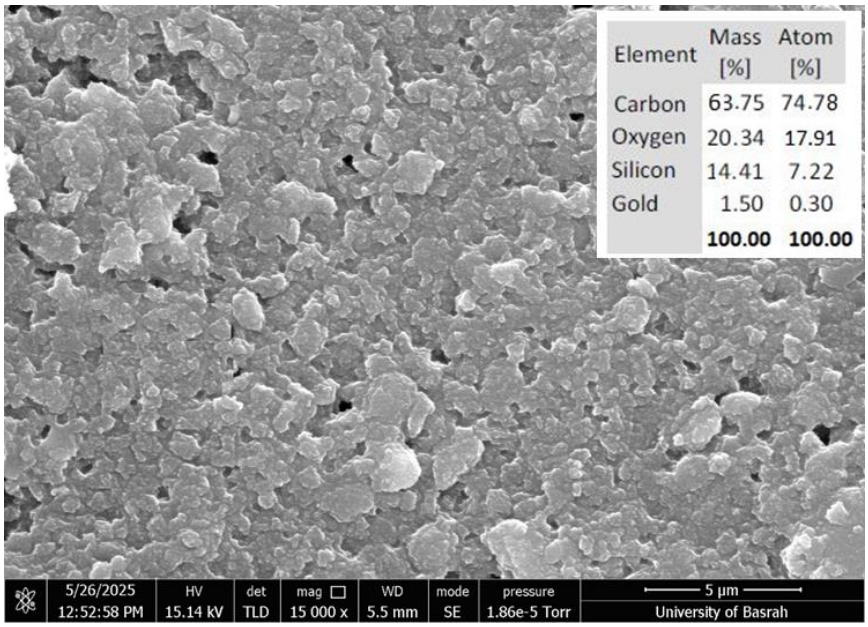


Figure 4. SEM-EDS of HRP Coating.

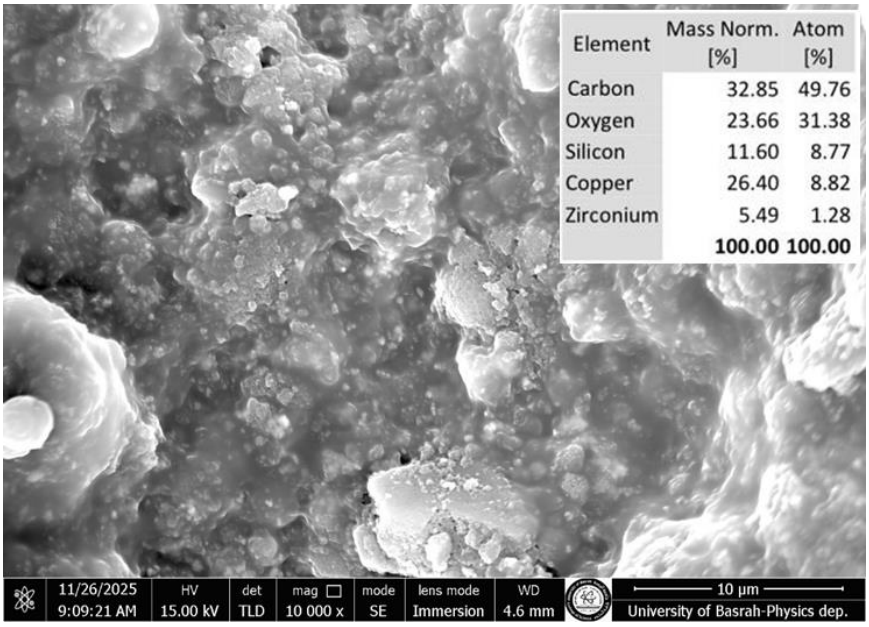


Figure 5. SEM-EDS of CuO/HRP Coating

Iron oxide nanoparticles have a strong tendency to cluster due to magnetic interactions and surface energy effects, as seen in the SEM image **(Fig. 6)**, which displays a heterogeneous and relatively compact surface with densely distributed fine particles and noticeable agglomeration within the polymer matrix **(Cornell and Schwertmann, 2003)**. With Fe (25.98 wt%) and O (20.33 wt%) as major constituents and carbon (33.35 wt%) representing the polymer matrix, EDS analysis verifies the incorporation of iron oxide and shows the formation of an organic–inorganic hybrid structure consistent with reported polymer–iron oxide systems **(Laurent et al., 2008)**. Particle clustering and dense morphology improve light scattering and increase effective interaction with incident radiation, which will be connected with further optical and thermal investigations and is anticipated to affect optical

absorption and photothermal response. In contrast to Fe_3O_4 coatings, the SEM image **(Fig. 7)** shows a heterogeneous surface with irregular agglomerated clusters, micro-voids, and apparent roughness within the polymer matrix, suggesting a less compact structure. Because of their high surface energy and anisotropic growth tendency, MnO_2 particles tend to form loosely packed aggregates, which is consistent with this morphology **(Post, 1999)**. With Mn (31.09 wt%) and O (23.13 wt%) as significant components and carbon (33.54 wt%) representing the polymer matrix, EDS analysis verifies the incorporation of manganese oxide and shows the creation of an organic–inorganic hybrid structure. In the following sections, optical and photothermal performance will be connected with the porous and agglomerated morphology, which enhances surface roughness and introduces various scattering sites that can affect light interaction and energy absorption.

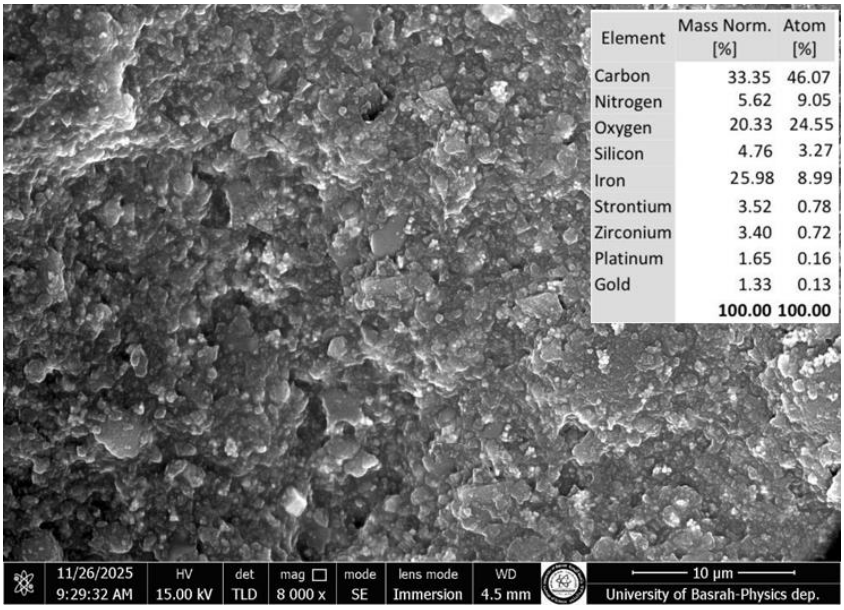


Figure 6. SEM-EDS of Fe_3O_4/HRP Coating.

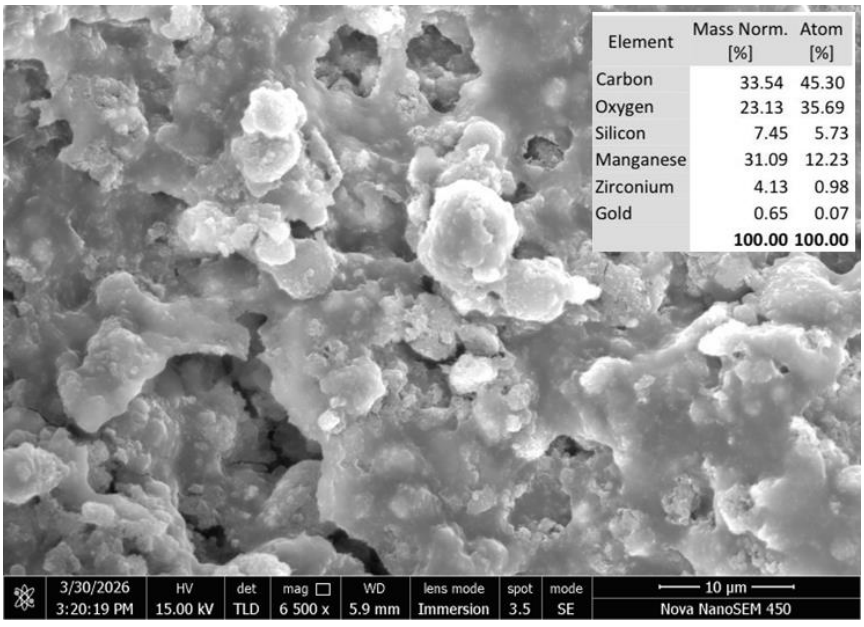


Figure 7. SEM-EDS of MnO_2/HRP Coating.

Compared to oxide-based coatings, which show Ni clusters of nanometric dimension dispersed over a continuous polymeric matrix with little agglomeration, the SEM image **(Fig. 8)** shows a finer and more uniform particulate structure. This is a relatively uniform distribution which is suitable for the behavior of nickel nanoparticles and the continuity of the active domain inside the coating which is associated with the size and surface of the nanoparticles **(Goldstein et al., 2018; E Silva et al., 2024)** .The EDS analysis also confirms a good incorporation of Ni, carbon (20.80 wt%, 41.93 at%) being assigned to the polymer matrix, while Ni is the main metallic element (48.93 wt%, 20.17 at%), indicating that a metallic–polymeric composite is formed, and not simply discrete deposits. This is a dense, and somewhat ordered, dispersion that provides a large number of metallic domains that enhance the interaction between light and matter at the nanoscale, as reflected by the better optical absorption and photothermal response observed in later investigations of Ni/HRP **(West et al., 2010)**.

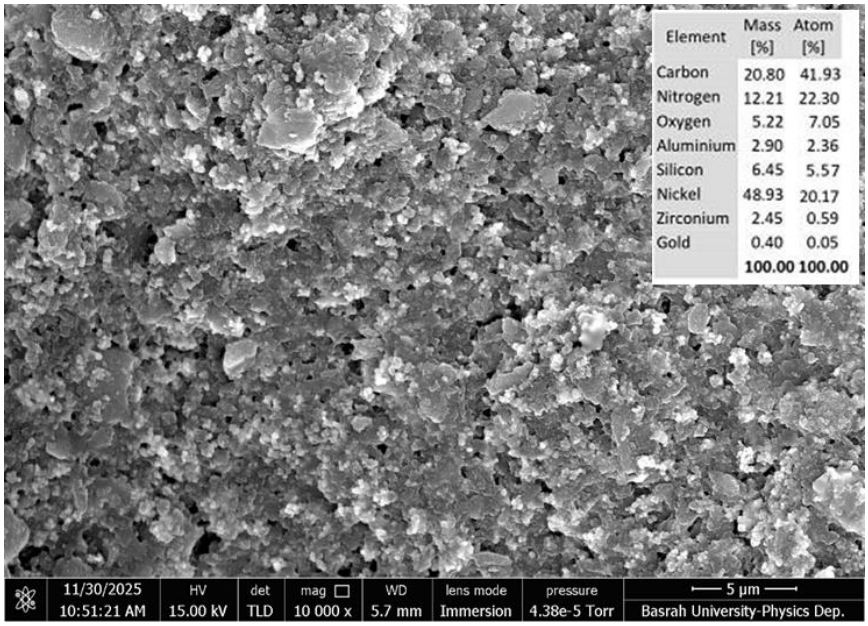


Figure 8. SEM-EDS of Ni/HRP Coating.

The SEM image **(Fig. 9)** shows a less uniform distribution of Ni/HRP and the presence of larger agglomerates with identifiable porosity in the polymer matrix. The high surface energy causes aggregation and reduces the continuity of the active domains, typical of oxide-based fillers **(Goldstein et al., 2018)**. Elemental distribution studies via EDS showed that NiO is present in similar atomic proportions to the other elements studied along with carbon from the polymer matrix, indicating the formation of a nickel oxide phase and not of metallic Ni. This separation is important as NiO exhibits semiconducting properties by charge transfer and interband transitions rather than free-electron plasmonic properties **(Rao and Raveau, 1998; Powell and Jablonski, 2011; Biesinger, 2017)**. The comparatively low optical and photothermal performance, which is caused by semiconducting type processes of absorption, is always attributed to the agglomerated and less homogeneous microstructure resulting in lower continuity of active domains.

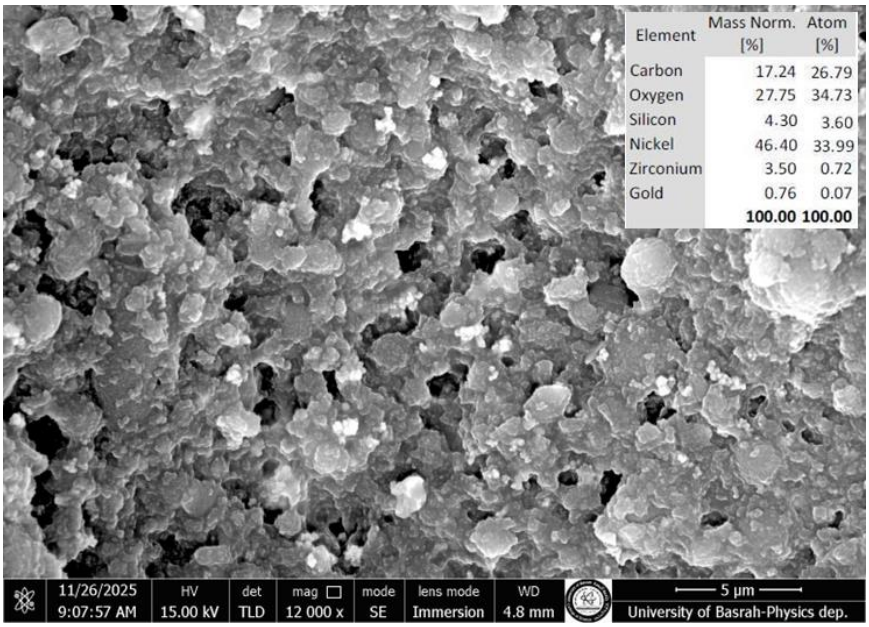


Figure 9. SEM-EDS of NiO/HRP Coating.

The optical response of the coatings is a combined effect of electronic structure, spectral properties and morphology. The spectral absorptance area under the curve (AUCα), as shown in **Fig. 10**, is a quantitative approximation of the overall solar harvesting efficiency. The absorption peak of Ni/HRP is located at 540 nm with relatively narrow full-width at half-maximum (FWHM = 95 nm) and a high peak-to-baseline ratio (see **Table 2**). The corresponding photon energy was calculated from the peak wavelength using $E\ (eV) = 1240/\lambda_p(nm)$. This is consistent with plasmon-like absorption behavior associated with the free-electron response of metallic Ni nanoparticles **(West et al., 2010; Naik et al., 2013; Somlyai-Sipos et al., 2019)**. The behavior is consistent with SEM-EDS images that show surface roughness characteristics, and an apparently uniform distribution of nanoscale metallic particles that are likely to facilitate plasmon-assisted light interaction. The morphology observed at the nanoscale provides structural conditions favorable for plasmonic phenomena, where the typical condition is that the particle diameter is in the order of magnitude of a fraction of the wavelength of the incident light. The presence of a deep and clear "valley" (or a peak in absorbance) within the solar range of the reflectance curve is consistent with plasmon-like optical behavior. In addition, the energy dissipated at the nanoparticles sites was also concentrated, which may have contributed to a much larger equilibrium temperature of the receiver than obtained with standard black paint. The prominent absorption feature in the visible range and the notable rise in equilibrium temperature in comparison to the base HRP coating, which suggests increased localized energy dissipation at the nanoparticle locations, further support the plasmon-like behavior. Ni successfully converts solar radiation into useful energy through a mechanism that may involve plasmon-assisted absorption, as evidenced by the high total AUCα = 1.717, as shown in **Table 3**, which is dominated by the visible contribution (1.241). NiO/HRP, on the other hand, has a comparatively sharp UV absorption peak at 302 nm with FWHM = 45 nm, which could be the result of interband charge-transfer transitions **(Sawatzky and Allen, 1984)**. An agglomerated oxide structure with minimal electronic continuity is revealed by SEM–EDS analysis, which is compatible with wide-bandgap behavior and absorption that is mostly

limited to the UV region. Despite the substantial UV contribution (0.262), this is reflected in the comparatively low total AUCα value (0.527), suggesting that a significant portion of absorption comes from the UV spectrum. NiO/HRP's narrow spectrum coverage limits its overall solar harvesting and photothermal conversion performance because the majority of solar energy is concentrated in the visible and near-infrared ranges. Similarly, O2p → Mn3d transitions are linked to a UV-dominant peak at 263 nm (FWHM = 55 nm) in MnO_2/HRP **(Devaraj and Munichandraiah, 2008; Cockayne and Li, 2012)**. The porous and loosely packed structure shown in the SEM measurements further restricts the effective absorption paths. Consequently, it has an overall AUCα of only 0.263, which suggests a weak spectral overlap with the bands of the visible and near-infrared. The CuO/HRP composite, however, exhibits a very wide absorption line (FWHM > 200 nm) at 520 nm, which could be attributed to oxygen vacancies and defect related electronic states on the surface, resulting in the extended visible-light absorption features **(Tripathi et al., 2020; Shaw et al., 2022)**. SEM-EDS confirms a heterogeneous and defect-rich structure, which may increase absorption over a wider spectral range by promoting sub-bandgap transitions and introducing mid-gap states. Despite this broadband behavior, its total AUCα of 0.146 is the lowest of all coatings, indicating that spectral widening alone might not provide efficient integrated solar energy harvesting. Fe_3O_4/HRP, which is linked to ligand-to-metal charge transfer, has a UV-dominant peak at 318 nm with a broad profile (FWHM >150 nm) extending into the visible region **(Fontijn et al., 1997; Rocha and Toma, 2002)**. A dense clustered architecture that improves multiple scattering and optical path length is revealed by SEM–EDS research. A moderate total AUCα of 0.325 is the result, indicating balanced but constrained spectrum coverage. Lastly, due to π→π* transitions in organic chromophores, the HRP coating displays a broad absorption peak at 670 nm with FWHM >180 nm and high intensity **(Lakowicz, 2006; Valeur and Berberan-Santos, 2012)**. SEM–EDS revealed a continuous polymeric matrix, which may have limited conductive pathways. The absorption behavior is primarily linked to electronic transitions in organic chromophoric groups within the polymer matrix rather than free-electron or plasmon-assisted mechanisms, thereby limiting effective photothermal conversion, even though it achieved the highest total AUCα = 2.636, driven by strong visible (1.607) and near-infrared (0.810) contributions. The UV–Vis data are presented as relative spectral absorptance in arbitrary units (a.u.), rather than absolute absorptance or logarithmic absorbance.

Table 2. UV-Vis absorptance data

Material	Peak λ (nm)	Peak Energy (eV)	FWHM (nm)	Peak Intensity (a.u.)	Baseline (a.u.)	Peak/ Baseline Ratio	Absorption Mechanism
Ni/HRP	540	2.23	95	5.47	2.07	2.64	Consistent with LSPR
NiO/HRP	302	4.10	45	1.72	0.66	2.61	Interband CT
MnO_2/HRP	263	4.70	55	0.56	0.33	1.71	Bandgap CT
CuO/HRP	520	2.41	>200	0.29	0.18	1.59	Defect-mediated
Fe_3O_4/HRP	318	4.08	>150	0.41	0.33	1.26	LMCT
HRP	670	1.92	>180	5.25	2.04	2.57	Molecular π→π*

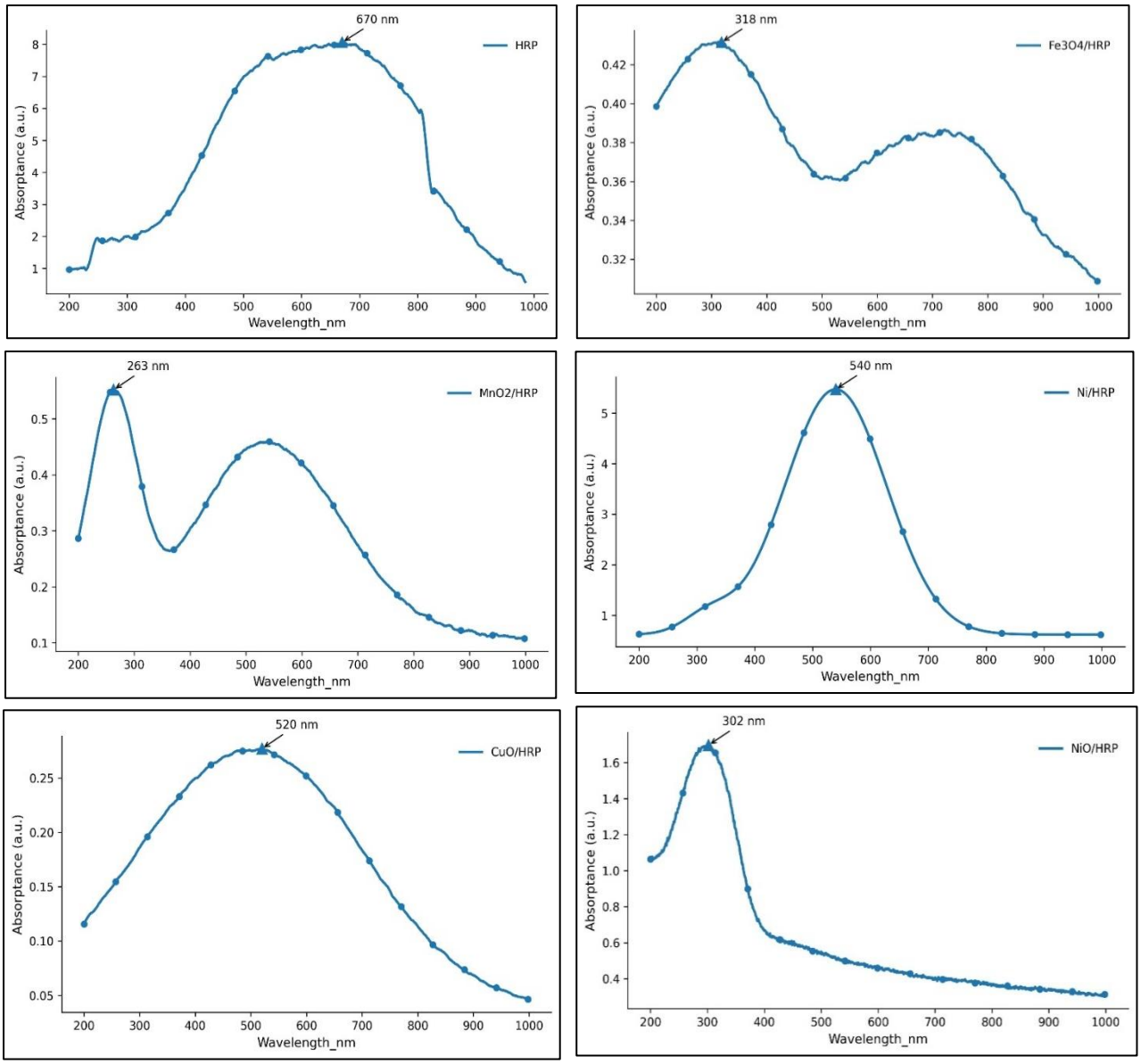


Figure 10. UV-Vis absorptance of Metal and Metal-oxide base coatings.

The spectral area under the curve (AUCα) was calculated using the trapezoidal numerical integration method over the specified wavelength intervals. The integrated values were scaled by a factor of 10^{-3} for numerical presentation and are reported in a.u.·nm.

Table 3. Spectral absorptance area under the curve from the UV-Vis Data

Coating	200-400 nm	400-700 nm	700-1000 nm	AUCα (Total) $\times 10^{-3}$ nm
HRP	0.218	1.607	0.81	2.636
Ni/HRP	0.21	1.241	0.266	1.717
NiO/HRP	0.262	0.158	0.108	0.527
Fe_3O_4/HRP	0.086	0.129	0.11	0.325
MnO_2/HRP	0.081	0.128	0.053	0.263
CuO/HRP	0.038	0.078	0.03	0.146

Thermal performance study provides a direct indicator of photothermal conversion efficiency by displaying the progressive evolution of substrate temperature and heating rate indicator in **Figs. 11 and 12** and **Table 4**. The thermal behavior depicted in **Figs. 11 and 12** was driven by the combined influence of spectral absorption properties and microstructural attributes, as characterized in Sections 3.3–3.4 and through SEM–EDS analysis, respectively.

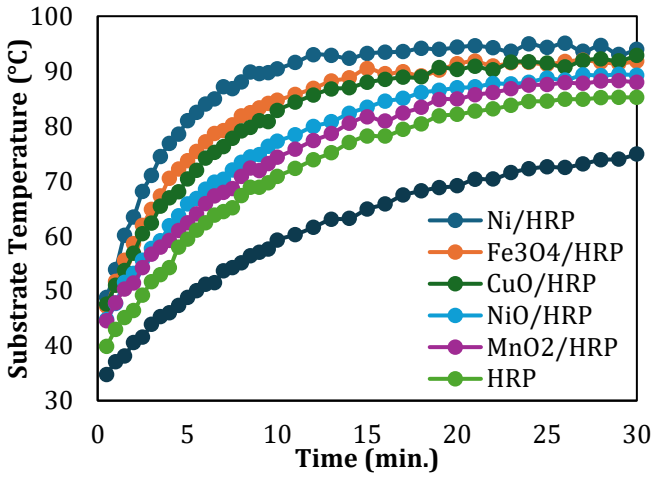


Figure 11. The photo-thermal conversion of the composite coatings in terms of the substrate temperature versus time of exposure to solar radiation

The quantitative thermal parameters are summarized in **Table 4** and reported as mean ± standard deviation (SD) from three replicate measurements (n = 3). The Ni/HRP coating exhibited the highest thermal performance with Q_t = 213.10 J, T_s = 93.93°C, and η_h = 0.360. A visible-region peak at λ_p = 540 nm, a narrow FWHM = 95 nm, and a high AUCα = 1.717—all of which are compatible with plasmon-like behavior—may be linked to this improved response. A comparatively uniform dispersion of metallic nanoparticles was previously established by SEM–EDS analysis, which may favor effective electron oscillation and quick photon-to-heat conversion via electron–phonon coupling **(Chen et al., 2010; Link and El-Sayed, 2000)**. The fast-heating rate indicator and the maximum thermal energy stored are explained by the close relationship between structure, optical response, and energy conversion. Despite a lower heating rate indicator (η_h = 0.195), CuO/HRP obtained the second-highest energy storage (Q_t = 209.20 J) at T_s = 92.85°C. Optical study confirms that this behavior is clearly related to its defect-mediated mechanism and extraordinarily broad absorption band (FWHM >200 nm), where low peak intensity is compensated for by broadband absorption. A heterogeneous and defect-rich morphology with uneven particle domains and localized structural discontinuities was identified by SEM–EDS studies. This morphology may bring defect-related electronic states that expand light absorption over a larger spectrum range. However, heterogeneous morphology may diminish the coating's heat transfer efficiency in comparison to more evenly dispersed structures, leading to a slower initial thermal response **(Zayed, 2024; Devaraj and Munichandraiah, 2008)**. With Q_t = 205.36 J, T_s = 91.78°C, and η_h = 0.267, Fe_3O_4/HRP demonstrated balanced performance, in line with its modest AUCα = 0.325 and LMCT-based optical absorption. A dense clustered shape that may improve multiple scattering and optical path length was revealed by SEM-EDS research **(Fontijn et al., 1997; Rocha and Toma, 2002)**. Due to their limited AUCα values (0.527 and 0.263) and UV-dominated optical absorption (λ_p = 302 nm and 263 nm), NiO/HRP and MnO_2/HRP demonstrated somewhat inferior thermal performance (Q_t = 196.29 J, 191.62 J; T_s = 89.26°C, 87.96°C; η_h = 0.216, 0.184, respectively). Agglomerated and

porous materials with poor electronic continuity were confirmed by SEM-EDS, which limited energy transfer and the efficient use of the solar spectrum **(Devaraj and Munichandraiah, 2008)**. Despite having the highest AUCα (2.636), the HRP coating performs the worst across coated samples (Q_t = 181.73 J, T_s = 85.21°C, η_h = 0.166). SEM–EDS study of a continuous polymer matrix confirms that this apparent contradiction is explained by its molecular absorption mechanism (π→π* transitions) and the lack of conductive channels. Thermal performance is not solely determined by absorption magnitude, as evidenced by the inefficient conversion of absorbed energy into heat **(Valeur and Berberan-Santos, 2012)**. The effectiveness of nanoparticle-enhanced coatings is confirmed by the Energy Enhancement Factor (ε_Q), which measures performance in relation to uncoated aluminum and shows improvements of 47.5% (Ni), 44.8% (CuO), 42.1% (Fe_3O_4), 35.9% (NiO), 32.6% (MnO_2), and 25.8% (HRP). By separating the coating contribution, the ΔQ_t study **(Fig. 13)** provides a physically meaningful comparison, with Ni exhibiting the highest net energy gain (~68.6 J), followed by CuO and Fe_3O_4 **(Kalogirou, 2014)**. The normalized energy representation Q_t* **(Fig. 14)** emphasizes early-stage performance disparities to further resolve transient behavior. Ni/HRP shows the quickest energy buildup (Q_t* ≈ 0.73) at t ≈ 5 min, followed by Fe_3O_4 (Q_t* ≈ 0.63) and CuO (Q_t* ≈ 0.54), while NiO (Q_t* ≈ 0.49) and MnO_2 (Q_t* ≈ 0.45) respond more slowly. This ranking remains valid at t ≈ 10 min, suggesting that early-time behavior controls material differentiation. At longer times (t > 25 min), all coatings converge toward similar steady-state values, indicating that variances are mostly caused by energy conversion rate rather than final storage capacity **(Zayed, 2024)**.

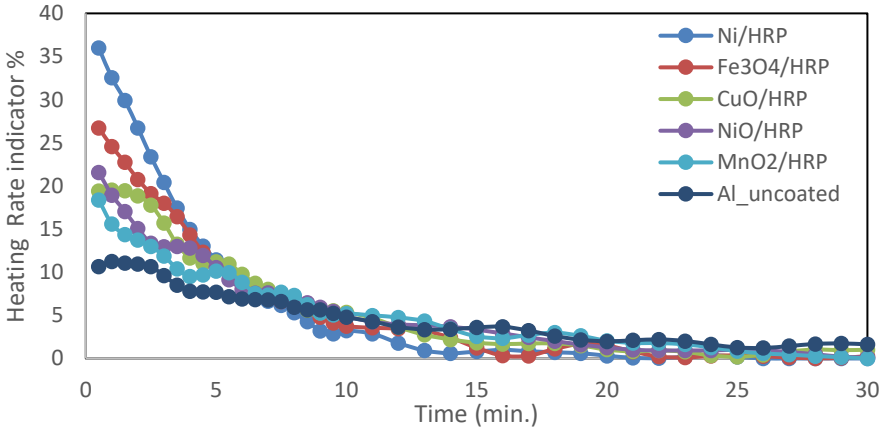


Figure 12. Heating Rate indicator (η_h) over time period.

Table 4. Quantitative Thermal Parameters

Material	T_s(°C), Mean ± SD	η_h, Mean ± SD	Q_t(J), Mean ± SD	Energy Enhancement Factor
Ni/HRP	93.93 ± 1.00	0.360 ± 0.018	213.10 ± 3.60	1.475
Fe_3O_4/HRP	91.78 ± 0.85	0.267 ± 0.015	205.36 ± 3.06	1.421
CuO/HRP	92.85 ± 1.00	0.195 ± 0.013	209.20 ± 3.60	1.448
NiO/HRP	89.26 ± 0.85	0.216 ± 0.014	196.29 ± 3.06	1.359
MnO_2/HRP	87.96 ± 0.75	0.184 ± 0.012	191.62 ± 2.70	1.326
HRP	85.21 ± 0.70	0.166 ± 0.011	181.73 ± 2.52	1.258
Al (uncoated)	74.87 ± 0.65	0.112 ± 0.009	144.48 ± 2.34	1.000

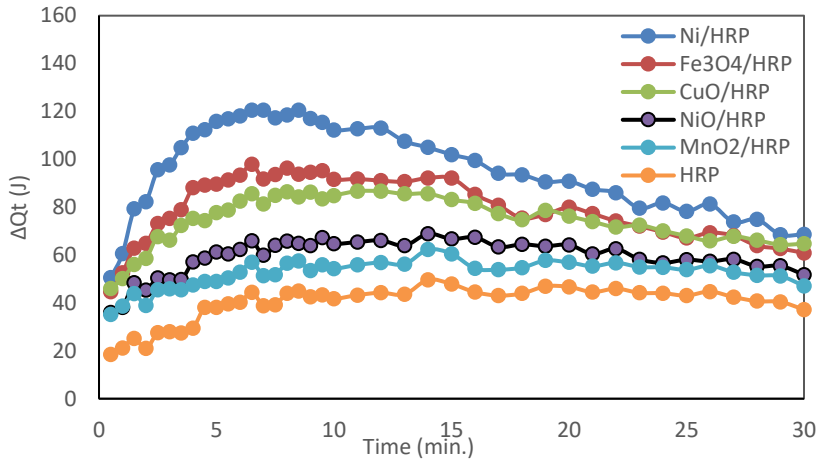


Figure 13. Incremental stored energy (ΔQ_t) vs Time.

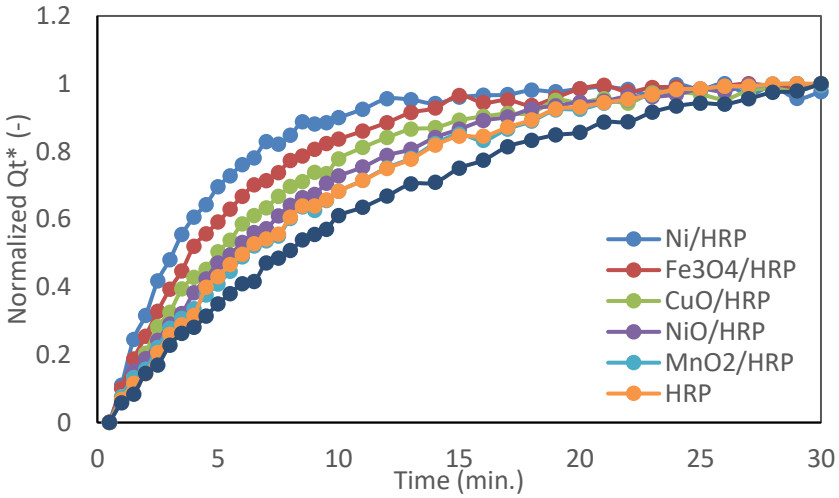


Figure 14. Normalized stored thermal energy Q_t^* vs Time.

The reduced-temperature analysis **(Fig. 15 and Table 5)** was employed to assess thermal performance under varying operating conditions, providing insight into thermal-loss trends and enabling a more reliable comparison of the photothermal behavior of different coatings. Spectral absorption and nanoscale energy transfer processes are coupled to control photothermal performance. Strong instantaneous and cumulative performance potentially associated with plasmon-like absorption and effective electron–phonon coupling was demonstrated by Ni/HRP. Ni/HRP exhibited the highest intercept ($\eta_0 = 0.501$) but the lowest reduced-temperature area under the curve ($AUC\theta = 0.837$). While CuO/HRP ($\eta_0 \approx 0.282$) maintained sustained thermal performance possibly through defect-mediated broadband absorption associated with oxygen vacancies and localized electronic states that extend visible-light harvesting over a wider spectral range, Fe_3O_4/HRP displayed a balanced behavior ($\eta_0 \approx 0.357$) possibly associated with mixed-valence charge-transfer mechanisms **(Tripathi et al., 2020; Shaw et al., 2022)**. However, because of UV-limited absorption, NiO and MnO_2 have lesser efficiency ($\eta_0 \approx 0.238$ and 0.200), while HRP ($\eta_0 \approx 0.186$) is still the least efficient possibly due to limited conductive pathways. According to traditional solar thermal theory **(Duffie and Beckman, 2013)**, the larger FRUL (6.29 $Wm^{-2}K^{-1}$) for Ni/HRP indicates significant thermal losses at increasing temperatures.

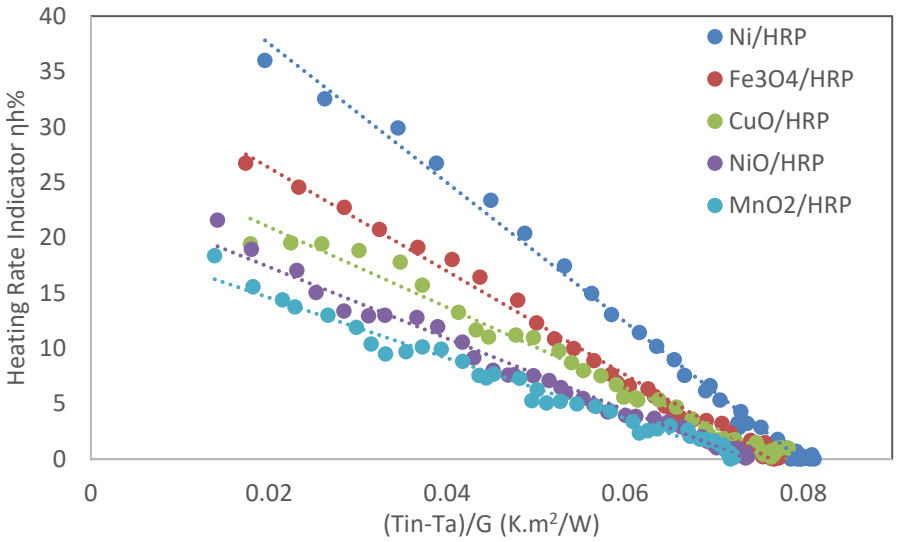


Figure 15. Reduced Temperature profile.

Table 5. Efficiency Parameters

Coating	η_0	FRUL	AUC_θ
Ni/HRP	0.501	6.287	0.837
Fe_3O_4/HRP	0.356	4.672	1.085
CuO/HRP	0.282	3.623	1.812
NiO/HRP	0.238	3.226	1.947
MnO2/HRP	0.200	2.725	2.083
HRP	0.185	2.637	2.238
Al_uncoated	0.116	1.983	2.241

Results of the specular reflectance measurements **(Table 6)**, confirm the optical–thermal consistency of the investigated coatings. For the opaque Al substrate and coating/Al systems, transmittance was negligible ($T \approx 0$). Therefore, $\alpha = 1 - R - T$ reduces to $\alpha \approx 1 - R$. In the present measurement configuration, R represents the measured specular reflectance; therefore, the reported absorptance values were estimated from the measured specular reflectance. Uncoated aluminum showed the highest reflectivity (70.4%) and lowest absorptance (29.6%), while HRP coating led to reflectivity of 7.2% (absorptance 92.8%), consistent with its broad visible absorption as observed in UV–Vis spectra. Incorporation of nanomaterials was found to enhance the photo-thermal conversion characteristics, with Ni/HRP achieving the lowest reflectivity (4.6%) and highest absorptance (95.4%). This directly correlates with its visible peak (λ_p = 540 nm), high AUCα, and uniform metallic dispersion observed in SEM–EDS, which confirms its superior thermal performance (T_s, Q_t, η_h). Due to broadband absorption processes supported by dense (Fe_3O_4) and defect-rich (CuO) structures in SEM–EDS, Fe_3O_4/HRP (94.7%) and CuO/HRP (94.5%) exhibit comparable high absorptance, which is compatible with their strong thermal responsiveness. On the other hand, NiO (93.8%) and MnO_2 (93.5%) have higher reflectivity, which is consistent with their agglomerated structures, lower AUCα, and UV-dominated absorption, all of which lead to lower photothermal efficiency. Overall, the absorptance trend: "Ni">"Fe_3O_4"≈"CuO">"NiO">"MnO_2" directly supports the UV–Vis and thermal results, demonstrating that photothermal performance is controlled by reduced

reflectivity (greater absorptance) when combined with an appropriate microstructure and absorption mechanism. Because diffuse reflection was excluded from the measurement configuration, the reported absorptance values are estimates based on specular reflectance and may overestimate the actual absorptance.

Table 6. Absorptance of Coatings as estimated from the specular reflectance measurements.

Coating	Beam Irradiance (W/m^2)	Reflected Intensity (W/m^2)	Reflectivity (%)	Absorptance (%)
Al substrate	963	678	70.4	29.6
HRP	954	69	7.2	92.8
Ni/HRP	952	44	4.6	95.4
Fe_3O_4/HRP	951	50	5.3	94.7
CuO/HRP	950	52	5.5	94.5
NiO/HRP	952	59	6.2	93.8
MnO_2/HRP	953	62	6.5	93.5

The collected characteristics (AUC_α, λ_p, FWHM, Q_t, η_h, and T_s) were used to create a Pearson correlation matrix **(Fig. 16)** in order to objectively assess the correlations between optical and thermal parameters. AUC_α did not correlate significantly with Q_t or η_h, suggesting that the photothermal performance is not solely dependent on the absorptance of the spectrum, but on the interplay of optical properties, absorption mechanisms and coating microstructure. On the other hand, there is little association between thermal indicators and peak wavelength (λ_p), indicating that peak position by itself has little effect on total energy conversion.

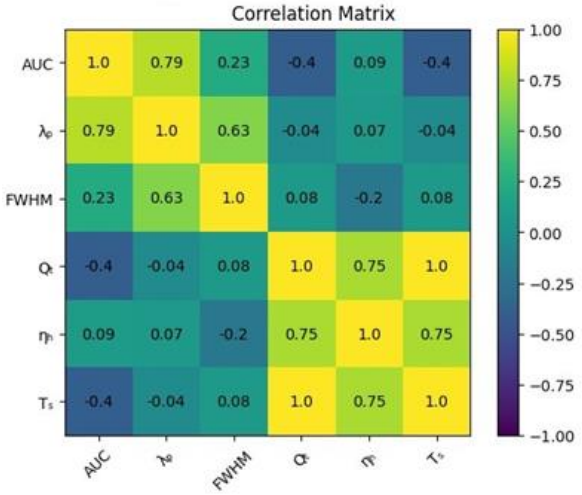


Figure 16. Pearson Correlation matrix.

The same applies for FWHM; there were no significant correlations with the thermal indicators, the spectrum bandwidth is not enough to explain the photothermal performance. This interpretation is completely consistent with the previously described concepts, according to which broadband absorption and effective light-matter interaction—enhanced by suitable microstructure (SEM–EDS)—rather than localized spectrum features dictate thermal behavior. There were no statistically significant correlations between AUCα and Q_t or between AUC_α and η_h for the spectra **(Figs. 17a and 17b)**, and the results indicated that the energy storage and the energy absorption rate are not solely related to the cumulative

spectral absorptance. On the other hand, their lesser and secondary influence is seen in the increased scatter in FWHM and λ_p correlations **(Figs. 17c and 17d**). The overall correlation analysis suggests that no individual spectral parameter act as a single dominant parameter for photothermal performance, favoring the interpretation based on the dual impact of the optical properties and the absorption processes and coating microstructure.

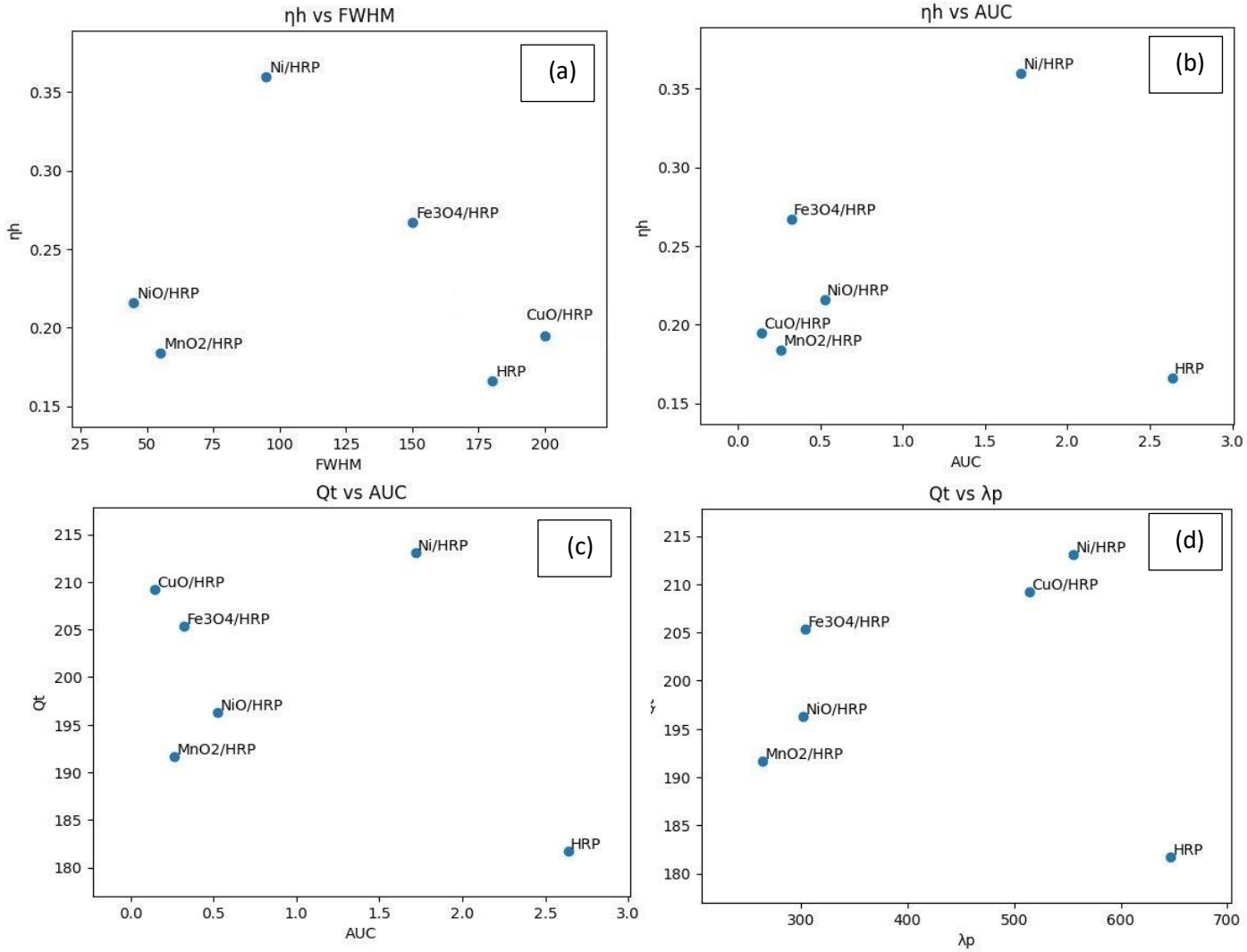


Figure 17. Quantitative Feature-Response Mapping of Spectral Parameters Governing Photo-Thermal Response.

The Pearson and Spearman correlation analysis of the key optical and thermal parameters are summarized in **Table 7**, and the corresponding p-values are provided for each parameter at significance level ($p < 0.05$; $n = 6$). The results suggest that there are no statistically significant relationships between AUCα and thermal response, suggesting that optical and structural properties may both contribute and energy conversion aspects play a combined role in the photothermal performance. For the thermal–thermal relationships, Q_t–T_s showed a statistically significant correlation using both Pearson and Spearman analyses ($p < 0.001$), whereas Q_t–η_h and η_h–T_s were significant only according to Spearman analysis ($p = 0.042$) and not according to Pearson analysis ($p = 0.087$). Given the limited number of coating types ($n = 6$), the absence of statistically significant correlations between spectral and thermal parameters should be interpreted cautiously and does not necessarily imply the absence of underlying relationships.

Table 7. Statistical Correlation Analysis of Key Photothermal Parameters

Relationship	Pearson r	Pearson $p-value$	Spearman ρ	Spearman $p-value$
$AUC_\alpha - Q_t$	-0.404	0.427	-0.257	0.623
$AUC_\alpha - \eta_h$	0.095	0.858	0.029	0.957
$AUC_\alpha - T_s$	-0.404	0.427	-0.257	0.623
$Q_t - \eta_h$	0.748	0.087	0.829	0.042
$Q_t - T_s$	1.000	<0.001	1.000	<0.001
$\eta_h - T_s$	0.748	0.087	0.829	0.042

4. CONCLUSIONS

The current work shows that the combined interaction between microstructure, optical absorption properties, and energy conversion mechanisms controls the photo-thermal performance of solar absorber coatings. When compared to the base HRP coating, the results clearly demonstrate that the addition of nanoparticles greatly improves thermal performance. The performance of the coatings was also strongly dependent on the type of additives and particle size. In terms of thermal performance, Ni/HRP exhibited the highest measured performance among the investigated coatings, while its strong visible-light absorption and high spectral absorptance were consistent with the proposed plasmon-like optical behavior. Its comparatively homogeneous microstructure, which promotes efficient energy transfer, supports this even more. In contrast, Fe_3O_4 and CuO achieved high performance through broadband absorption mechanisms, while NiO and MnO_2 showed a relatively lower efficiency due to their limited interaction with the solar spectrum. The correlation analysis revealed that none of the thermal parameters was statistically significant for AUCα, meaning that the thermal behavior is a result of a combination of spectral properties, absorption mechanisms, and the microstructure of the coating. Overall, the results show that high spectral absorption, effective energy conversion, and advantageous microstructural characteristics must all be integrated simultaneously to provide excellent photothermal performance. These results provide a clear foundation for the development of advanced solar-thermal coatings and demonstrate the critical importance of nanoscale engineering, particularly the application of metallic nanoparticles like nickel in enhancing solar energy conversion efficiency.

Credit Authorship Contribution Statement

Saleh K. Jabur: Conceptualization, formal analysis, methodology, project administration, resources, supervision, visualization, writing—review and editing. Ahmed A. Al-Tabbakh: data curation, validation. Laith. Al-Gebory: data curation, investigation, validation, writing—original draft preparation

Declaration of Competing Interest

The authors declare that they have no known competing financial interests or personal relationships that could have appeared to influence the work reported in this paper.

REFERENCES

Al-Obaidy, A.M.H., Fayyadh, E.M. and Al-Dabagh, A.M., 2024. Effect of nano and nanocomposite coating on pool boiling heat transfer. *Engineering and Technology Journal*, 42(7), pp. 1048–1060. https://doi.org/10.30684/etj.2024.149236.1742.

Biesinger, M.C., 2017. Advanced analysis of copper X-ray photoelectron spectra. *Surface and Interface Analysis*, 49(13), pp. 1325–1334. https://doi.org/10.1002/sia.6239.

Cao, G., 2004. *Nanostructures and Nanomaterials: Synthesis, Properties and Applications*. Imperial College Press, London. http://dx.doi.org/10.1142/9781860945960.

Chen, H., Shao, L., Ming, T., Sun, Z., Zhao, C., Yang, B. and Wang, J., 2010. Understanding the photothermal conversion efficiency of gold nanocrystals. *Small*, 6(20), pp. 2272–2280. https://doi.org/10.1002/smll.201001109.

Cockayne, E. and Li, L., 2012. First-principles DFT + U studies of the atomic, electronic, and magnetic structure of α-MnO_2 (cryptomelane). *Chemical Physics Letters*, 544, pp. 53–58. https://doi.org/10.1016/j.cplett.2012.06.061.

Cornell, R.M. and Schwertmann, U., 2003. *The Iron Oxides: Structure, Properties, Reactions, Occurrences and Uses*. 2nd ed. Wiley-VCH. https://doi.org/10.1002/3527602097.

Cullity, B.D. and Stock, S.R., 2001. *Elements of X-ray Diffraction*. 3rd ed. Prentice Hall, Upper Saddle River, NJ.

Dawood, N.I., Jalil, J.M. and Faraj, S.R., 2025. Thermal performance enhancement of solar collectors by nanoparticles and magnetic field: a review. *Engineering and Technology Journal*, 43(1), pp. 75–93. https://doi.org/10.30684/etj.2024.152986.1809.

Devaraj, S. and Munichandraiah, N., 2008. Effect of crystallographic structure of MnO_2 on its electrochemical capacitance properties. *Journal of Physical Chemistry C*, 112(11), pp. 4406–4417. https://doi.org/10.1021/jp7108785.

Duffie, J.A. and Beckman, W.A., 2013. Solar Engineering of Thermal Processes. 4th ed. Wiley, Hoboken, NJ. https://doi.org/10.1002/9781118671603.

E Silva, F.A., Salim, V.M.M. and Rodrigues, T.S., 2024. Controlled Nickel nanoparticles: A review on how parameters of synthesis can modulate their features and properties. *AppliedChem*, 4(1), pp. 86–106. https://doi.org/10.3390/appliedchem4010007.

Farchado, M., San Vicente, G., Barandica, N., Sánchez-Señorán, D. and Morales, Á., 2024. High performance selective solar absorber stable in air for high temperature applications. *Solar Energy Materials and Solar Cells*, 271, P. 112849. https://doi.org/10.1016/j.solmat.2024.112849.

Farooq, S.A., Raina, A., Mohan, S., Singh, R.A., Jayalakshmi, S. and Ul Haq, M.I., 2022. Nanostructured coatings: Review on processing techniques, corrosion behaviour and tribological performance. *Nanomaterials*, 12(8), P. 1323. https://doi.org/10.3390/nano12081323.

Fontijn, W.F.J., van der Zaag, P.J., Devillers, M.A.C., Brabers, V.A.M. and Metselaar, R., 1997. Optical and magneto-optical polar Kerr spectra of Fe_3O_4 and Mg^{2+}- or Al^{3+}-substituted Fe_3O_4. *Physical Review B*, 56, pp. 5432–5442. https://doi.org/10.1103/PhysRevB.56.5432.

Goldstein, J.I., Newbury, D.E., Michael, J.R., Ritchie, N.W.M., Scott, J.H.J. and Joy, D.C., 2018. *Scanning Electron Microscopy and X-Ray Microanalysis*. 4th ed. Springer. https://doi.org/10.1007/978-1-4939-6676-9.

Granqvist, C.G., 2007. Transparent conductors as solar energy materials: A panoramic review. *Solar Energy Materials and Solar Cells*, 91(17), pp. 1529–1598. https://doi.org/10.1016/j.solmat.2007.04.031.

Kalogirou, S.A., 2014. *Solar Energy Engineering: Processes and Systems*. 2nd ed. Academic Press, London. https://doi.org/10.1016/C2011-0-07038-2.

Kennedy, C.E., 2002. Review of Mid- to High-Temperature Solar Selective Absorber Materials. National Renewable Energy Laboratory (NREL), Report No. NREL/TP-520-31267, Golden, CO, USA. https://doi.org/10.2172/15000706.

Kumar, K.K.P., Atchuta, S.R., Prasad, M.S., Barshilia, H.C. and Sakthivel, S., 2024. Review on selective absorber coatings: A catalyst for enhanced solar energy conversion efficiency. *Solar Energy Materials and Solar Cells*, 277, 113080. https://doi.org/10.1016/j.solmat.2024.113080.

Lakowicz, J.R., 2006. *Principles of Fluorescence Spectroscopy*. 3rd ed. Springer. https://doi.org/10.1007/978-0-387-46312-4.

Laurent, S., Forge, D., Port, M., Roch, A., Robic, C., Vander Elst, L. and Muller, R.N., 2008. Magnetic iron oxide nanoparticles: Synthesis, stabilization, vectorization, physicochemical characterizations, and biological applications. *Chemical Reviews,* 108(6), pp. 2064–2110. https://doi.org/10.1021/cr068445e.

Link, S. and El-Sayed, M.A., 2000. Shape and size dependence of radiative, non-radiative and photothermal properties of gold nanocrystals. *International Reviews in Physical Chemistry*, 19(3), pp. 409–453. https://doi.org/10.1080/01442350050034180

Liu, B., Wang, C., Bazri, S., Badruddin, I.A., Orooji, Y., Saeidi, S., Wongwises, S. and Mahian, O., 2021. Optical properties and thermal stability evaluation of solar absorbers enhanced by nanostructured selective coating films. *Powder Technology*, 377, pp. 939–957. https://doi.org/10.1016/j.powtec.2020.09.040.

Naik, G.V., Shalaev, V.M. and Boltasseva, A., 2013. Alternative plasmonic materials: beyond gold and silver. *Advanced Materials*, 25(24), pp. 3264–3294. https://doi.org/10.1002/adma.201205076.

Paredes, J.I. and Burghard, M., 2004. Dispersions of individual single-walled carbon nanotubes of high length. *Langmuir*, 20(12), pp. 5149–5152. https://doi.org/10.1021/la049831z.

Post, J.E., 1999. Manganese oxide minerals: Crystal structures and economic and environmental significance. *Proceedings of the National Academy of Sciences*, 96(7), pp. 3447–3454. https://doi.org/10.1073/pnas.96.7.3447.

Powell, C.J. and Jablonski, A., 2011. NIST Electron Effective-Attenuation-Length Database. National Institute of Standards and Technology (NIST).

Rao, C.N.R. and Raveau, B., 1998. *Transition Metal Oxides*. Wiley-VCH.

Rashid, H.J., Sultan, K.F. and Anead, H.S., 2022. Thermal performance of an evacuated-tube solar collector using nanofluids and an electrical curtain controlled by an artificial intelligence technique. *Engineering and Technology Journal*, 40(1), pp. 8–19. https://doi.org/10.30684/etj.v40i1.2021.

Reimer, L. and Kohl, H., 2008. *Transmission Electron Microscopy: Physics of Image Formation*. 5th ed. Springer. https://doi.org/10.1007/978-0-387-40093-8.

Rocha, R.C. and Toma, H.E., 2002. Electron transfer in inorganic mixed-valence systems. *Química Nova*, 25(4), pp. 624–638. https://doi.org/10.1590/S0100-40422002000400018.

Sawatzky, G.A. and Allen, J.W., 1984. Magnitude and origin of the band gap in NiO. *Physical Review Letters*, 53(24), pp. 2339–2342. https://doi.org/10.1103/PhysRevLett.53.2339.

Selvakumar, N. and Barshilia, H.C., 2012. Review of physical vapor deposited (PVD) spectrally selective coatings for mid- and high-temperature solar thermal applications. *Solar Energy Materials and Solar Cells*, 98, pp. 1–23. https://doi.org/10.1016/j.solmat.2011.10.028.

Shaw, M., Samanta, D., Bera, S., Mahto, M.K., Shaik, M.A.S., Konar, S., Mondal, I., Dhara, D. and Pathak, A., 2022. Role of surface oxygen vacancies and oxygen species on CuO nanostructured surfaces in model catalytic oxidation and reductions: Insight into the structure–activity relationship toward the performance. *Inorganic Chemistry*, 61(37), pp. 14568–14581. https://doi.org/10.1021/acs.inorgchem.2c01467.

Somlyai-Sipos, L., Czagány, M., Janovszky, D. and Baumli, P., 2019. Synthesis and investigation of nickel nanoparticles. Proceedings of the 5th World Congress on New Technologies (NewTech'19), Lisbon, Portugal, 2019. https://doi.org/10.11159/icnfa19.118.

Tripathi, A., Dixit, T., Agrawal, J. and Singh, V., 2020. Bandgap engineering in CuO nanostructures: Dual-band, broadband, and UV-C photodetectors. *Applied Physics Letters*, 116(11), P. 111102. https://doi.org/10.1063/1.5128494.

Valeur, B. and Berberan-Santos, M.N., 2012. *Molecular Fluorescence: Principles and Applications*. 2nd ed. Wiley-VCH. https://doi.org/10.1002/9783527650002.

Wang, H., 2021. Structure, optical properties and thermal stability of all-ceramic solar selective absorbing coatings: A mini review. *Frontiers in Energy Research*, 9, 789917. https://doi.org/10.3389/fenrg.2021.789917.

West, P.R., Ishii, S., Naik, G.V., Emani, N.K., Shalaev, V.M. and Boltasseva, A., 2010. Searching for better plasmonic materials. *Laser & Photonics Reviews*, 4(6), pp. 795–808. https://doi.org/10.1002/lpor.200900055.

Williams, D.B. and Carter, C.B., 2009. *Transmission Electron Microscopy: A Textbook for Materials Science*. 2nd ed. Springer. https://doi.org/10.1007/978-0-387-76501-3.

Xu, K., Du, M., Hao, L., Mi, J., Yu, Q. and Li, S., 2020. A review of high-temperature selective absorbing coatings for solar thermal applications. *Journal of Materiomics*, 6(1), pp. 167–182. https://doi.org/10.1016/j.jmat.2019.12.012.

Zayed, M.E., 2024. Recent advances in solar thermal selective coatings for solar power applications: technology categorization, preparation methods, and induced aging mechanisms. *Applied Sciences*, 14(18), 8438. https://doi.org/10.3390/app14188438.

الاقتران البصري–الحراري الشبيه بتأثيرات البلازمون في طلاءات الماصات الشمسية النانوية المصممة هندسيًا: تحليل متكامل للبنية والخصائص الطيفية والتحويل الفوتوحراري

صالح خضير جبر[1]، *، أحمد عبد الرحمن الطباخ[2]، ليث إسماعيل الجبوري[3]

[1]قسم التقنيات الميكانيكية، المعهد التقني البصرة، الجامعة التقنية الجنوبية، البصرة، العراق

[2]قسم الفيزياء، كلية العلوم، جامعة النهرين، بغداد، العراق

[3]كلية هندسة المواد، الجامعة التكنولوجية، بغداد، العراق

الخلاصة

يتضمن هذا العمل تحضير طلاءات ماصة فوتوحرارية مدعمة بإضافات نانوية وتوصيفها لتطبيقات التحويل الفوتوحراري. كما يتناول دراسة العلاقة بين إضافة الجسيمات المعدنية وأكاسيد المعادن والخواص البصرية للطلاءات المركبة وخصائصها في التحويل الفوتوحراري. تم توصيف الطلاءات المحتوية على Ni وFe_3O_4 وCuO وNiO وMnO_2 باستخدام تقنيات SEM–EDS ومطيافية UV–Vis ضمن المدى (200–1000 nm) وقياسات الانعكاسية المرآتية، إضافةً إلى إخضاعها لتحليل فوتوحراري زمني. أظهرت الطلاءات المدعمة بالنيكل أفضل أداء مقارنةً ببقية الطلاءات، إذ حققت أعلى درجة حرارة سطح بلغت 93.93 °م وخزن حراري مقداره 213.10 J مع أعلى قيمة لمؤشر معدل التسخين بلغت 0.360، مترافقًا مع قمة امتصاص في المجال المرئي عند نحو 540 nm. كما حققت امتصاصية تكاملية مرتفعة بلغت نحو 1.717 وانعكاسية منخفضة مقدارها 4.6%. وقد يرتبط هذا الأداء بآليات امتصاص شبه–بلازمونية محتملة في جسيمات النيكل النانوية، قد تسهم في تعزيز تحويل الفوتونات إلى حرارة. كما أظهرت الطلاءات المحتوية على Fe_3O_4 وCuO أداءً تنافسيًا نتيجة آليات الامتصاص واسع النطاق، في حين بينت الطلاءات المحتوية على NiO وMnO_2 كفاءة أقل بسبب هيمنة الامتصاص في نطاق الأشعة فوق البنفسجية. وعلى الرغم من الامتصاصية العالية للطلاء الأساسي، بقيت استجابته الحرارية محدودة، وقد يرتبط ذلك بمحدودية مسارات التوصيل الحراري. يشير تحليل الارتباط إلى أن الأداء الفوتوحراري لا تحكمه معلمة طيفية منفردة، وإنما يتأثر بالتفاعل المشترك بين الخصائص البصرية والحرارية والبنيوية للطلاءات. وتشير النتائج إلى أن الأداء الفوتوحراري قد يتأثر بالتفاعل المشترك بين الامتصاص واسع النطاق وآليات الامتصاص شبه–البلازمونية أو المرتبطة بالعيوب البنيوية المحتملة، إلى جانب خصائص البنية المجهرية المناسبة.

الكلمات المفتاحية: الطلاءات المركبة، البنى النانوية، الخواص البصرية، التحويل الفوتوحراري، الطلاءات الماصة الفوتوحرارية، الأداء الحراري.